Self-similar length-displacement scaling achieved by scale-dependent growth processes: Evidence from the Atacama Fault System

A. Stanton-Yonge*[a], J. Cembrano[b,c], W.A. Griffith[d], E. Jensen[e,f] and T.M. Mitchell[a]

[a] Department of Earth Sciences, University College London, 5 Gower Street, London, WC1E 6BT, UK

[b] Department of Structural and Geotechnical Engineering, Pontificia Universidad Católica de Chile, Vicuna Mackenna 4860, Santiago, Chile

[c] Andean Geothermal Center of Excellence (CEGA, FONDAP-CONICYT), Santiago, Chile

[d] School of Earth Sciences, The Ohio State University 275 Mendenhall Laboratory, 125 South Oval Mall, Columbus, OH 43210-1308.

[e] Departamento de Ciencias Geológicas. Universidad Católica del Norte. Avda. Angamos 0610, Antofagasta, Chile

[f] EJS Geología E.I.R.L. Altos del Mar 1147, Antofagasta

*Corresponding author: Ashley Stanton-Yonge (ashley.sesnic.18@ucl.ac.uk), (+44) 7542545258, 5 Gower Street, London, WC1E 6BT, UK.

Abstract

The complex process of tip-propagation and growth of natural faults remains poorly understood. We analyse field structural data of strike-slip faults from the Atacama Fault System using fracture mechanics theory to depict the mechanical controls of fault growth in crystalline rocks. We calculate the displacement-length relationship of faults developed in the same rock type and tectonic regime, covering a range of five orders of magnitude, showing a linear scaling defined by $\boldsymbol{d_{max}} = 0.0337L^{1.02}$. A multiple linear regression approach based on the cohesive end zone (CEZ) crack model was formulated to estimate the range of possible effective elastic moduli, cohesive endzone lengths, stress drops, and fracture energies from displacement distributions mapped on natural faults. Our results challenge the existent paradigm wherein the self-similarity of fault growth is only achieved under the condition of invariable stresses and elastic properties. We propose a model of self-similar fault growth with scale-dependent evolution of shear modulus, cohesive end zone length and stress drop. These results also have implications for determination of stress drop for small earthquakes that are consistent with recent advances in observational seismology.

1 Introduction

The process by which faults propagate into previously unfaulted rock is controlled by local stresses, friction and material response near faults, but its mechanical nature remains poorly understood. Understanding how faults propagate trough the Earth's crust is fundamental for unraveling the processes governing brittle deformation, which in turn has strong implications in a variety of fields such as earthquake nucleation and seismic hazard assessment, fracture distribution and fluid flow through the upper crust.

Geologists have been widely interested in finding scaling relationships between geometrical parameters of faults such as length, maximum displacement and damage zone width (*e.g*. Walsh and Watterson 1979; Cowie and Scholz 1992b; Faulkner et al., 2011). These relationships aim to link field observations to mechanical models and thus unravel the processes governing fault development over geologic time. Some of these models (*e.g*. Cowie and Scholz 1992a,b; Scholz 1993) predict that faults grow in a self-similar manner under conditions of invariable stress and material properties, which results in linear scaling between fault length (L) and maximum displacement (d_{max}). However, the multiple datasets collected over the past decades (*e.g*. Walsh and Watterson, 1988; Marrett and Allmendinger, 1991; Cowie and Scholz, 1992a; Dawers et al. 1993; Schlische et al. 1996; Kim and Sanderson, 2005) have not reached consensus regarding the relationship between L and d_{max}. This divergence of opinion is associated with several limitations inherent to the data collection of length and displacement of natural faults (*e.g*. Kim and Sanderson 2005). It has been suggested that these limitations can only be reduced by spanning the widest range of scales as possible, on faults developed under the same rock type and stress regime (Cowie and Scholz 1992b; Scholz 1993; Gillespie et al. 1992).

Here, we build on previous observations by Cembrano et al. (2005), Jensen et al. (2011), Mitchell and Faulkner (2009) and Faulkner et al. (2011) to study the mechanical controls involved in fault growth as depicted from the geological record. We focus on strike-slip faults of the Atacama Fault System (Central Andes, Chile) developed on relatively isotropic, low-porosity, dioritic and meta-dioritic rocks over scales ranging from centimeters to kilometers to provide new insights into the progressive development of upper crustal faults in crystalline rocks. We measure the along-strike slip distributions and the displacement-length relationship of faults in the study area, covering a range of five orders of magnitude. We then formulate a multiple linear regression approach based on the cohesive end zone (CEZ) crack model (Cowie and Scholz, 1992a, Burgmann et al., 1994) to analyze our field data and invert for fault tractions from mapped slip distributions. Our combined approach provides valuable evidence supporting the self-similarity of the fault growth process. which we propose is achieved by scale-dependent parameter evolution (*i.e.*, shear modulus, end zone length and stress drop) throughout the development of a fault system. These findings have strong implications in the understanding of the mechanics of fault growth and provides a valuable tool for estimating geometrical parameters of faults under various scales.

2 Fault development and scaling

2.1 Fault initiation and propagation

The lifetime of a fracture may be subdivided into initiation, propagation, and cessation (Pollard and Segall, 1987), and relative displacements may accumulate along the fracture throughout this process. The understanding of fault initiation and propagation in crystalline rocks is largely influenced by the classical work of Segall and Pollard (1983) and Martel et al. (1988) – among others – who regarded natural faults (variably mixed Mode II-III, shear fractures) as nucleating from earlier joints (Mode I fractures) because of stress reorientation and subsequent linkage via wing cracks at their tips. This interpretation is consistent with the observation that shear cracks cannot propagate in their own plane in otherwise isotropic materials (*e.g.*, Erdogan and Sih, 1963; Cotterell and Rice, 1980), but grow from the reactivation of pre-existing discontinuities under a rotating stress field or from the coalescence of pre-rupture tension cracks (*e.g.*, Scholz et al. 1993; Crider and Peacock, 2004; Healy et al. 2006).

In a study of a strike-slip duplex system in dioritic rocks in the Coastal Cordillera of Chile,Jensen et al. (2011) showed that mesoscopic faults did not initiate from pre-existing joints formed under a previous stress field. They propose that faults likely grew by the progressive propagation and coalescence of small tension fractures in the same regional stress field, a process that finally led to cataclastic rocks within larger, mature fault zones in a way similar to that suggested by Crider and Peacock (2004) and Laubach et al. (2014). Faults grew as composite fault zones linked by secondary faults or extension fractures forming duplexes at millimeter to kilometer scale. Although the evidence to deduce such evolution has been mainly observed at microscopic- and outcrop-scales, it can also be inferred to occur at larger scales, as the system is geometrically self-similar (Jensen et al., 2011). This fault maturation via progressive incorporation of fractures agrees with previous laboratory observations wherein shear fracture propagation occurs by linkage and localization of opening mode fractures that form in the process zone of the main fracture (Lockner et al., 1991; Zang et al. 2000, Anders et al. 2014, Aben et al. 2019).

2.2 Fault growth models

Classic Linear Elastic Fracture Mechanics (LEFM) models of cracks subjected to uniform stress drop (*e.g.*, Pollard and Segall 1987) predict an elliptical fault slip distribution (Figure 1a) with an abrupt termination of slip at the crack terminations. This maximum displacement gradient at the crack tips results in infinite stresses in the vicinity of the fault terminations, which is physically impossible. Therefore, the LEFM crack model is insufficient for unravelling near-tip deformation and fault growth in nature.

Cowie and Scholz (1992a) addressed the infinite stress issue by adapting a cohesive end zone (CEZ) model of a Mode I crack (Dugdale, 1960; Barrenblatt, 1962; Goodier and Field, 1963) to study Mode II fault growth. In this model, inelastic yielding occurs in a small region surrounding the fault tips, within an otherwise elastic medium. In CEZ models, the inelastic yielding is simulated by applying cohesive traction, equal to the yield strength of the material σ_y, along the fault from the fault tips to a finite distance inward. The cohesive traction resists the crack-driving stress such that the net stress intensity factor, *i.e.*, the sum of contributions arising from the uniform stress drop and the cohesive tractions, is zero at the crack tips, ensuring a finite near-tip fault stress field that does not exceed the strength of the rock. As a result, the displacement profile predicted by the model tapers out gradually towards the crack tip (Figure 1b).

Burgmann et al. (1994) explored a similar CEZ model where, rather than adopting the Mode I equations derived by Barenblatt (1962), they simulate the non-linear stress distribution by summing solutions of stresses and displacement arising from stress functions for various fault traction distributions (Tada et al. 1973, p. 5.11). For the simple, symmetric CEZ model comparable to that of Cowie and Scholz (1992a), the crack is segmented into a central area characterized by a well-developed fault with lower strength, and an immature zone at the fault terminations with increased resistance to slip due to either inelastic deformation and/or greater friction between fault surfaces (*e.g.*, Palmer and Rice 1973). The desired stress distribution is simulated by superimposing three loading configurations: (1) A stress-free crack under uniform remote loading stress τ_r, (2) a uniform residual stress of magnitude τ_f along the central, mature portion of the fault, and (3) uniform stress of magnitude τ_{cez}, equal to the shear strength of the surrounding medium, along the cohesive end zone at the terminations of the crack. Certain distributions of shear stress in the cohesive end zone of a shearing-mode crack will oppose the action of the remotely applied load, resulting in total stress intensity factor zero (*i.e.*, $K_{II}^{total} = K_{II}^{r} + K_{II}^{CEZ} = 0$) and thus eliminating the stress singularity at the faults tips.

The slip distribution resulting from this CEZ model is, in its general case, similar in shape to that of Cowie and Scholz 1992a (Figure 1b) and is controlled by the three shear stress magnitudes τ_r, τ_f, τ_{CEZ}, the length of the end zone, and the elastic properties of the medium. Burgmann et al. (1994) also explored other factors influencing slip distributions along faults, showing that variable stress, splay fracturing, fault interaction and variable elastic properties in the medium alter the otherwise symmetric, bell-shaped slip distributions along faults. Similar results are shown by Peacock and Sanderson (1996) by accounting for variabilities in fault propagation rates, due to, for example, fault interaction, which they suggest could explain much of the diversity identified in slip distribution profiles.

The concavely tapering slip towards the crack tips in the CEZ model (Figure 1b) is a result of the explicit representation of yielding occurring directly along the plane of the crack (Scholz, 2019). However, abundant field (*e.g.*, Vermilye and Scholz, 1998; Mitchell and Faulkner 2009; Faulkner at al., 2011) and experimental evidence (*e.g.*, Pollard and Segall, 1987; Lockner et al., 1991; Moore and Lockner, 1995; Zang et al., 2000) shows that inelastic deformation occurs within a volume surrounding fault tips rather than the idealized strip explicitly represented by analytic CEZ models. Numerical elastic-plastic models such as Constant Fault Tip Taper (CTTP) (*e.g.*, Kanninen and Popelar 1985, Scholz and Lawler, 2004) instead allow yielding to occur in a volume around the fault tip. A direct consequence of this model is that slip distribution profiles taper linearly toward the fault tips (Figure 1c), a feature supported by displacement profiles from most exhumed faults (Muraoka and Kamata, 1983, Cowie and Shipton, 1998; Gupta and Scholz 2000; Scholz and Lawler 2004 and references therein) and earthquake slip distributions (Manighetti et al., 2005). The CTTP model does not permit an analytical formulation, although Burgmann et al. (1994) showed that similar slip distributions can be achieved by linearly varying tractions along the fault plane (Figure 1c).

Here we are interested in assessing the key mechanical parameters governing fault growth and how they can be depicted from the geological record. We thus consider the CEZ model from Burgmann et al. (1994) the most suitable analytical tool to interpret our field evidence. Similar results and insights may be obtained by implementing a similar procedure using fault models with contributions from linearly varying tractions.

Insert Figure 1.

2.3 Fault scaling

As slip accumulates along a fault, the stress concentration at its tips increases. If near-tip stresses meet the appropriate propagation criterion, the fault must then increase its length to relax the resulting stress concentrations and remain in quasi-static equilibrium. The relationship between maximum displacement d_{max} and length L is thus a key indicator of the fault growth process, as it provides a description of fault development over geologic time.

The relationship between d_{max} and the maximum linear dimension of the fault surface (L) has been defined as follows (*e.g.*, Walsh and Watterson, 1988; Marrett and Allmendinger, 1991; Cowie and Scholz, 1992b; Dawers et al., 1993):

$$d_{max} = cL^n \qquad (1)$$

The mechanical CEZ model by Cowie and Scholz (1992a) predicts that a fault loaded by a uniform remote stress grows in a self-similar process such that:

$$d_{max} = \frac{C(\sigma_0 - \sigma_f)L}{\mu} \qquad (2)$$

Where σ_0 is the shear strength of the surrounding rock, μ is the shear modulus, and σ_f the frictional shear stress on the fault, C a constant that depends on the ratio of the remote stress loading the fault to the rock shear strength. This model predicts linear scaling ($n = 1$ in equation 1) between d_{max} and L, with the constant of proportionality varying with lithology and tectonic environment.

However, over the last three decades different authors have obtained n values between 0.5 and 2 (*e.g.*, Walsh and Watterson, 1988; Marrett and Allmendinger, 1991; Cowie and Scholz, 1992a; Dawers et al. 1993; Schlische et al. 1996; Kim and Sanderson, 2005), raising questions regarding the underlying physical origin of such wide range of n values and scatter.

The relationship between maximum displacement (d_{max}) and fault length (L) is poorly constrained for exhumed fault datasets for several reasons. Most available datasets mix either different types of faults or different types of rocks, which adds to the inherent complexity of fault nucleation and propagation processes. Furthermore, the coexistence of brittle and plastic deformation mechanisms at individual faults (*e.g.*, Griffith et al. 2009) can severely impact the interpretation of the $\frac{d_{max}}{L}$ ratio. Another common limitation comes from the difficulty of covering the full spectrum of fault geometries across different scales. With a few exceptions (*e.g.*, Walsh and Watterson, 1988; Gillespie et al., 1992; Schlische et al., 1996; Bistacchi et al., 2011), most studies performed at the same rock type and tectonic regime cover a range of scales of less than 3 orders of magnitude. According to Gillespie et al. (1992), the effect of most of these fundamental limitations can be significantly reduced by covering a range of spatial scales greater than five orders of magnitude.

Additionally, there are practical problems associated with measuring displacements and lengths from 2D fault outcrops. Displacement measurements rely on markers displaced by faults; however, to measure displacement from offset between two points of a marker, the measure needs to be made on a line parallel to the slip vector. Uncertainty regarding the slip vector of faults leads to underestimation of displacement. Another unavoidable shortcoming for almost all possible fault studies arises from measuring geometrical parameters from the arbitrarily exposed trace or section of a fault. Faults in 2D are idealized as planar surfaces with an elliptical tip-line boundary representing zero displacement, with increasing displacement towards the surface center. Thus, the exposed fault trace will unlikely represent its section of maximum length and displacement, instead, fault traces correspond to chords of their elliptical surfaces at an unknown distance of their center. Hence, fault traces measurements will yield, as a rule, a*pparent* length and displacements (*e.g*. Kim and Sanderson 2005, Griffith et al., 2009). However, because in this idealistic representation of faults both length and displacement decrease elliptically towards the fault terminations, the apparent length and displacements of an arbitrarily exposed trace of a fault will decrease in the same proportion with respect to the fault center. As a result, the d_{max}/L ratio should not be significantly affected by this geometrical bias.

3. Field data

3.1 Case study

To examine the fault slip patterns at various scales, we have mapped subvertical strike-slip faults that developed in a similar, nearly isotropic rock type covering five orders of magnitude, ranging from centimeters to a few kilometers. All mapped faults are part of the Caleta Coloso Duplex (CCD) (Figure 2) in the Atacama fault system (AFS), an intra-arc shear zone active during the Mesozoic (*e.g*., Brown et al., 1993; Scheuber and Gonzalez, 1999).

The CCD is formed by two, NNW-striking, subvertical master faults: the Bolfin and Jorgillo Faults, which are in turn joined by a set of second-order NW-striking, imbricate splay faults (Figure 2)

(González, 1996, Cembrano et al. 2005). The second-order faults in the CCD have steep dips and dominantly left-lateral displacement; they have minimum net displacements varying between 10 and 100 m and show variable internal structure. Centimeter to meter-long sinistral strike slip faults occur within several kilometric splay faults at the southern termination of the Bolfin fault. Some of these splays consist of segments of centimeter to meter-long faults linked by shear/extensional fractures forming duplexes, whereas higher displacement faults (on the order of >10m) show well-developed layers of cataclasites and gouge (Cembrano et al. 2005). Additionally, the lack of any pre-existing regional-scale joint systems occurring in the area implies that faults in the strike-slip duplex grew by brittle fault propagation and coalescence in otherwise intact rock.

Insert Figure 2.

3.2 Field measurements of fault length and displacement and along-strike displacement profiles

Trace lengths ($\boldsymbol{L}$) and maximum exposed horizontal displacements ($\boldsymbol{d_{max}}$) were measured on more than one hundred, centimeter to kilometer-long sinistral strike slip faults (*i.e.*, lengths were measured parallel to the slip vector). Analyzed faults cut very similar, mostly isotropic dioritic and metadioritic rocks (Figure 2). Both rock types consist of 5-20 percent quartz, 40-60 percent plagioclase and a different proportion of mafic minerals (Hornblende, pyroxene, and biotite). $\boldsymbol{L}$ and $\boldsymbol{d_{max}}$ were obtained from two different sources, as follows:

1. High resolution satellite images (Figure 3b), which show faults previously mapped in the field (*e.g.*, Gonzalez, 1996; Jensen et al. 2011, Cembrano et al. 2005), reveal very well-defined, nearly straight traces of tens of meters to a few kilometers-long strike-slip faults with synkinematic slickenlines raking up to ~30°. These faults cut and displace a subvertical quartz-plagioclase, north-striking dyke, allowing the measurement of horizontal separations, which was performed on the central third of all mapped faults (Figure 3b)

2. The second source of data are direct observations and measurements on outcrops such as those shown in Figure 3a, c. Much care was placed on identifying both fault tips and the maximum horizontal offset on subvertical, strike-slip faults having subhorizontal to shallowly-plunging synkinematic striae. Subvertical magmatic layering, amphibolite dykes and chlorite veins lying nearly orthogonal to faults serve as excellent markers documenting both slip sense and magnitude. Outcrops cover a range of lengths from a few centimeters to tens of meters, covering two to three orders of magnitude; the same is the case for displacements, which range from a few to hundreds of millimeters.

Additionally, several displacement markers were identified along four outcrop-scale faults, allowing us to reconstruct their along-strike slip profiles.

Insert Figure 3.

3.3 Field results

The along-strike slip profiles for four outcrop-scale faults are plotted in Figure 4. They all show the largest displacement closer to the fault centre and an overall symmetrical displacement distribution with respect to the central maximum. Furthermore, displacement fault profiles 2 and 3 show a clear gradient decrease towards the tips, whereas faults 1 and 4 appear to have a linear decrease in slip towards the tips, although this could be due to a paucity of offset markers.

Insert Figure 4.

Out of more than one hundred faults mapped in the field, only sixty-three were selected for displacement –length analysis (data repository). These meet the following minimum conditions: (i) Subvertical dips, (ii) unequivocally exposed fault tips, and (iii) maximum exposed displacement measured from subvertical offset markers close to the fault center. Faults traces bounded by intersections with other faults were not considered for further analysis as they would likely underestimate maximum displacement with respect to total length.

The data is plotted on a single L versus d_{max} log-log diagram (Figure 5), with a power law fit of $\boldsymbol{d_{max}} = 0.0337L^{1.02}$, with coefficient of determination $R^2 = 0.94$. Although the data is clearly biased to small scale faults, it is evident that more scatter is found in faults that are shorter than around 1 m. Another important characteristic of our data set is the scarcity of data in the middle part of the range, particularly for fault lengths between 20 and 800 m.

Insert Figure 5.

4. Linear regression for shear traction inversion

4.1 Regression formulation

Below we formulate a linear regression approach based on the cohesive end zone (CEZ) crack model by Burgmann et al., (1994) to invert for shear tractions and end zone lengths from our mapped slip distribution profiles (Figure 4). By doing so, we evaluate the capability of the CEZ model to fit our measured faults and then analyze the parameters controlling the fault growth process. Figure 1b shows the geometry and boundary conditions of this model. A uniform remote stress τ_r acts along the length $2a$ of the fault. The well-developed or mature portion of the fault, of length $2d$ is subjected to a residual frictional stress τ_f whereas uniform stress of magnitude τ_{cez} act along the cohesive end zone from $d \leq x \leq a$ and $-a \leq x \leq -d$.

The slip distribution $D_x(x)$ for the plane strain mode II CEZ crack can be computed using the following terms (Burgmann et al., 1994).

$$D_x(x) = \frac{2(1-\nu)}{\mu}\left[\begin{array}{l} \left\{(\tau_r - \tau_{cez}) - (\tau_f - \tau_{cez})\frac{2}{\pi}\sin^{-1}\left(\frac{d}{a}\right)\right\}\sqrt{a^2 - x^2} \\ -\frac{1}{\pi}(\tau_f - \tau_{cez})\left\{\begin{array}{l} (d+x)\cosh^{-1}\left(\frac{a^2 + xd}{a|x+d|}\right) \\ +(d-x)\cosh^{-1}\left(\frac{a^2 - xd}{a|x-d|}\right) \end{array}\right\} \end{array}\right] \quad (3)$$

Here, μ is the shear modulus and ν the Poisson ratio of the elastic medium. This distribution reduces to the expected end-members, for example, as $(a - d) \rightarrow 0$, (3) becomes a classic crack with a uniform stress drop of τ_r-τ_f and an infinite stress concentration at the tips.

We use this closed form solution to use measured slip distributions $D_x(x)$ along four CCD faults (Figure 4) to explore the fault tractions and effective elastic moduli that may have governed fault growth. Because Cowie and Scholz (1992a) interpret the fault growth process as self-similar, they speculate that the actual length of the end zone $(a - d)$ increases with total fault length, a, and thus the scaled length of the end zone, $\frac{(a-d)}{a}$, is constant during fault growth. By assuming this and setting $\tau_f = 0$ (i.e., traction free, complete stress drop, along the well-developed portion of the fault), and non-dimensionalizing the spatial terms by a:

$$x^* = x/a$$

$$d^* = d/a$$

$$a^* = 1$$

we can rewrite (3) as:

$$D_x = C_1 F_1 + C_2 F_2 \quad (4)$$

where

$$F_1 = \sqrt{1 - \left(\frac{x^*}{a}\right)^2}$$

$$F_2 = \left(\frac{d^* + x^*}{a}\right)\cosh^{-1}\left(\frac{1 + \frac{x^* d^*}{a^2}}{\left|\frac{x^* + d^*}{a}\right|}\right) + \left(\frac{d^* - x^*}{a}\right)\cosh^{-1}\left(\frac{1 - \frac{x^* d^*}{a^2}}{\left|\frac{x^* - d^*}{a}\right|}\right)$$

$$C_1 = \frac{2(1-\nu)}{\mu}\left\{(\tau_r - \tau_{cez}) + \left(\frac{2\tau_{cez}}{\pi}\right)\sin^{-1}\left(\frac{d^*}{a}\right)\right\}$$

$$C_2 = \frac{2(1-\nu)\tau_{cez}}{\mu \quad \pi}$$

Rewriting equation (4) in matrix-vector form with n discrete fault slip measurements each at position x_n:

$$\begin{bmatrix} D_x(x_1) \\ \vdots \\ D_x(x_n) \end{bmatrix} = \begin{bmatrix} F_1(x_1) & F_2(x_1) \\ \vdots & \vdots \\ F_1(x_n) & F_2(x_n) \end{bmatrix} \begin{bmatrix} C_1 \\ C_2 \end{bmatrix} \qquad (5)$$

We can now solve for the unknown constants C_1 and C_2, and then compute the tractions τ_r and τ_{cez} from the relationships defined above.

4.2 Inversion results

Using the linear regression methodology described above, we invert for the shear tractions τ_r and τ_{cez} to fit our measured fault-slip profiles (Figure 4). Because the scaled end zone length $(a - d)/a$ is an unknown independent parameter in F_1 and F_2 , we perform inversions using a range of $(a - d)/a$, between 0 and 0.9. As an example of how results vary with scaled end zone length, Figure 6a shows the results of total stress intensity factor $K_{II}^{total} = K_{II}^{r} + K_{II}^{CEZ}$, where

$$K_{II}^{r} = \tau_r\sqrt{\pi a} \qquad (6)$$

$$K_{II}^{CEZ} = \frac{\tau_{cez}}{\pi}\sqrt{2\pi(a-d)} \quad (7)$$

These were calculated for each fault in the range of scaled end zone lengths and fixed values for the effective elastic moduli ($\mu = 1\ GPa\ , \nu = 0.25$). As we will show later in section 3.3, elastic properties must vary in some cases to satisfy the requirement of $K_{II}^{total} \approx 0$. For the CEZ model results to be physically meaningful, it is necessary that $K_{II}^{total} \approx 0$ to eliminate the stress singularity at the fault tips.

For short faults (*i.e.* fault 1, a=0.4m and fault 2, a=1.2m), the length of the CEZ does not exert much influence in the total stress intensity factor magnitude, and within all the range, $K_{II}^{total} \approx 0$. On the contrary, for fault 3 (a=2.3m), only CEZ length values above 0.55 result in $K_{II}^{total} \approx 0$, whereas for fault 4 (a=6.9m) small CEZ lengths, $(a-d)/a \approx 0.1$ result in the smallest K_{II}^{total}. For each fault we selected the magnitude of $(a-d)/a$ that result in stress intensity factor closest to zero. Figure 6b shows the resulting modelled slip distribution for each fault (dashed black) contrasted to the measured slip profiles (blue). The coefficient of determination for the fits range between 0.91 and 0.98 (Figure 6b).

Insert Figure 6.

4.3 Parameter estimation

Using the regression approach described in section 3.2., we can now investigate the parameters controlling the fault growth process. Regressions were conducted over a range of 100 possible shear moduli ranging from 0.1 GPa to 20 GPa and 100 possible relative end zone lengths $(a-d)/a$, from 0 to 0.9. Of these 10,000 regressions, we select the parameter combinations that satisfy the requirements of the CEZ models and have a satisfactory coefficient of determination. The criteria are:

i) $\left|K_{II}^{total}\right| < 15\ MPa$

ii) τ_{cez} within 15 MPa of the *in situ* shear strength (assumed to be 100MPa), and

iii) coefficient of determination for the regression of $R^2 > 0.8$.

Shear moduli

Figure 7(a) displays the shear moduli as a function of end zone length for the four faults, where each data point represents a combination of parameters that fit the above defined criteria. Best fit shear moduli magnitudes (up to 4 GPa) are lower than laboratory estimated values (up to 20 GPa for granodiorites). In general, shear moduli increase with end zone length for small faults (1 and 2), whereas for longer faults (3 and 4), the slip distributions can only be fit by a single, low value (μ<0.5 GPa). Furthermore, a general trend can be observed in which best fit shear moduli increase with decreasing fault length. Maximum fault displacement is also inversely correlated with shear modulus (Figure 7b).

Insert Figure 7.

Stress drop

The static stress drop associated with a slip event is defined as the difference between the remote field shear stress τ_r and the shear stress resolved on the fault after slip τ_f. In this case, we considered a complete drop with $\tau_f = 0$; therefore, shear stress drop magnitude equals that of the driving stress τ_r. Figure 8 shows the best fit τ_r as a function of end zone length for each of the modelled faults. Larger stress drops require larger end zone lengths. Also, longer faults are associated with larger stress drops. An exception for this general trend is fault 4, which has a similar maximum displacement to fault 3, though with three times its length (see Figure 4). For this fault, only two of the 10,000 parameter combinations result in a satisfactory CEZ model, characterized by very small end zone length and low stress drop.

Insert Figure 8.

Fracture Energy

The fracture energy G_c , or the critical energy release rate during the time of fracture propagation, is the energy consumed per unit area of fracture advance, and is closely related to the stress drop, but also to fracture length and to effective elastic modulus. It can be regarded as an estimate of the elastic strain energy released in creating the fault. G_c can be estimated from the stress intensity factor corresponding to the uniform applied stress, $(\tau_r - \tau_f)$ as follows for a plane strain CEZ crack (*e.g.*, Tada et al., 2000, p. 30.2):

$$G_c = \frac{(1-\nu^2)\left(K_{II}^{r}\right)^2}{E} \quad (8)$$

Figure 9 shows the calculated fracture energy G_c with respect to end zone length for our four faults. In general, more fracture energy is required for propagating cracks with longer endzone lengths. As predicted by Cowie and Scholz (1992) and Scholz (1993), G_c scales with fault length, with larger faults requiring higher fracture energy to propagate/slip. However, fault 4 violates this trend. We discuss the implications of these results in the following sections.

Insert Figure 9.

5 Discussion

5.1 Dmax vs L scaling

In a very influential work on the mechanics of fault scaling, Cowie and Scholz (1992b) stated the following as one main conclusion regarding the different relationships found between *L* and *d*: …. "*Finally, it must be stated that none of these data are really conclusive, otherwise it would not be possible for such a wide divergence of opinion to exist. What is needed is data that span a much greater scale range for faults in a single tectonic environment and rock type*".

Our dataset is, as far as we know, one of the few sets of d/L ratios coming from faults from the essentially same rock type and tectonic setting, covering a range of five orders of magnitude. Furthermore, the studied faults did not form from earlier joints but nucleated and propagated from the coalescence of tensile fractures under the same stress regime (Cembrano et al. 2005; Jensen et al. 2011). For a displacement to length ratio dataset to be geologically and mechanically meaningful, sampled faults should have not been formed from earlier joints because their initial length would be greater than zero.

Because the variables of rock type, regional stress regime, fault growth mechanics, and subsequent fault kinematics are essentially set constant in this study, the main sources of scatter for our data set probably arise from underestimations of lengths and/or displacement due to exposure limitations and non-horizontal slip vectors. Another very likely source of scatter probably arises from fault linkage which is associated with irregular along-strike displacement gradients (Cartwright et al., 1995; Cladouhos and Marrett 1999; Schlische et al., 1996*)*. For linked faults the displacement/length ratio will likely be underestimated. Although our displacement profiles (Figure 4) do not show the irregular gradients characterizing linked faults, it is not possible to rule out linkage as a fault growth mechanism in our dataset, especially for large faults (Rotevatn et al., 2019). However, it is interesting to note that scatter of our dataset is higher within the smaller scale faults (<1 m length). This can be attributed to the larger number of faults that is possible to map at this scale (*e.g*. Schlische et al., 1996). The scarcity of data in the middle part of the range, *i.e.* fault lengths between 20 and 800 m, is mostly associated with the absence of reliable displacement markers in this fault length range. Finally, permanent ductile deformation accompanying brittle fault displacement will also tend to overestimate the d_{max}/L ratio (Griffith et al., 2009). Although some limited ductile deformation is observed along some of the mapped faults, this effect is negligible for most cases (Cembrano et al. 2005).

The relationship between d_{max} and L obtained for this data set confirms a linear scaling between d_{max} and L, where the constant of proportionality varies with rock type and tectonic environment. The linear relationship between d_{max} and L is also shown by Schlische et al. (1996) in a compilation of d_{max} and L from different sources, covering eight orders of magnitude of faults from a variety of fault types and lithologies. However, the considerable scatter from this compilation suggests that the d_{max} vs L relationship would be better constrained by analysing data separately from each particular geological setting.

The d_{max}/L ratio (c from Equation 1) was defined by Cowie and Scholz (1992b) as a critical shear strain for fault propagation that determines the magnitude of the finite stress concentration at the ends of a growing fault. For this data set c is equal to 0.0337, and because it was calculated over a wide range of faults developed in the same rock and tectonic regime, we interpret it to be approximately representative of the development of the whole fault system. Below we analyse the mechanical significance of this quantity.

Equation 9 provides an analytical formulation to calculate the d_{max}/L ratio, where:

$$\frac{d_{max}}{2a} = \frac{(1-\nu)}{\mu}\left\{(\tau_r - \tau_{cez}) + \left(\frac{2\tau_{cez}}{\pi}\right)\sin^{-1}\left(\frac{d^*}{a}\right) + \frac{2\tau_{cez}}{\pi}\left(\frac{d^*}{a}\right)\cosh^{-1}\left(\frac{a}{d^*}\right)\right\} \qquad (9)$$

The d_{max}/L ratio thus depends on the elastic properties of the medium (ν, μ), the remote shear stress τ_r, the shear strength of the medium τ_{CEZ} and the relative end zone length $\frac{d^*}{a}$. By setting constant $\nu = 0.25$ and the shear strength $\tau_{CEZ} = 100MPa$, we calculate d_{max}/L using equation 6 with a range of relative end zone lengths from 0 to 1, a range of remote shear stress, $\tau_r = 20 - 100\ MPa$, and shear modulus $\mu = 0.2 - 1\ GPa$.

Figure 10 shows the d_{max}/L ratio as a function of end zone length for various combinations of τ_r and μ, represented by the τ_r/μ ratio. Increasing endzone lengths correlate with decreasing d_{max}/L ratios. Also, increasing d_{max}/L ratios are related to increasing shear moduli and decreasing remote shear stresses. This simple analysis shows that under the CEZ crack model framework, multiple combinations of end zone lengths, remote shear stress and shear moduli can result in the characteristic d_{max}/L ratio for our case study (c=0.0337, see in black line). In the following section we further discuss the implications of this observation.

Insert Figure 10.

5.2 Parameter evolution during fault growth

Our linear regression approach allowed us to model the slip distributions of all four measured faults (Figure 6b) using a Cohesive End Zone (CEZ) crack model. This supports the applicability of the fracture mechanics framework, in particular, of the CEZ model, for analysing field structural data and estimating the parameters controlling fault growth. Consequently, we estimated the ranges of end zone length and shear modulus that meet the requirements of the CEZ model and had a satisfactory coefficient of determination for each of our measured faults and calculated the static stress drop and fracture energy associated with them. It is important to note that the fit of the model to the measured slip distributions could be improved by considering linearly varying cohesive tractions at the end zone (Burgmann et al. 1994). However, we chose to implement the basic formulation of the CEZ model to identify the first order controls of fault growth.

Our calculations show that best fit shear moduli increase with decreasing fault length and with decreasing displacement (Figure 7a, b). We interpret this is a result of large faults being influenced by a larger area of the fractured surrounding medium, which reduces the effective shear modulus as compared to small faults propagating into comparatively more intact rock. This interpretation is consistent with the observation made at the same study area by Faulkner et al.

(2011) that fault damage zone widths scale with displacement. As faults grow and increase their length and cumulative displacement, their damage zone expands, which is reflected by the increase of micro and macrocrack damage. Significant changes in the elastic properties of crystalline rocks have been reported as crack damage accumulates (*e.g*. Faulkner et al., 2006; Heap and Faulkner 2008; Heap et al., 2009). Longer faults then propagate into a comparatively more damaged/fractured medium with reduced shear modulus.

However, if the process of fault growth decreases the effective elastic modulus of the medium, the general assumption of fault growth being self-similar only when the elastic properties and remote stress remain constant would be challenged. Our data set shows a self-similar system with fault length scaling linearly with displacement, and, at the same time, a parameter evolution where only reduced shear modulus can fit a CEZ crack model for longer faults. It is therefore necessary that a trade-off exists between fault growth parameters to preserve the self-similarity of the system.

As can be seen in Figure 7a, relative end zone length increases with fault length: longer faults seem to require a higher proportion of breakdown zone to propagate. Furthermore, Figure 10 shows that numerous different combinations of parameters may fit the characteristic d_{max}/L of the system; in particular, longer end zone lengths correlate with smaller shear moduli. Our results thus support the interpretation that as longer faults propagate within a medium with comparatively reduced effective modulus, the relative end zone length of the fault increases, thus preserving the self-similarity of the system. This suggests that the assumption of the CEZ model by Cowie and Scholz (1992a) of the relative length of the end zone $(a - d)/a$ being constant throughout the development of faults might not be accurate. In contrast, it seems that there is a trade-off between end zone length and elastic modulus over fault growth: as the effective elastic modulus decreases during the progressive fracturing of the medium, faults may increase end zone length to propagate.

The increasing proportion of end zone length in longer faults may be physically explained by several mechanisms. First, the inability of fractured damage zone rocks to sustain large stresses can lead to smearing out near-tip stress gradients. Second, it is widely known that fracture healing increases the shear strength of rocks (*e.g*. Tenthorey et al. 2003; Laubach et al. 2019), a process that has been interpreted to occur from the fracture tip inwards (Smith and Evans, 1984). Third, the CEZ model itself provided some mechanical and geometrical constraints that lead to the same interpretation.

According to the CEZ model, a fault at a growing stage i is characterized by a well-developed, low shear strength, segment of length $2d_i$ and an end zone length of $2s_i$. Once it propagates, fault length increases into $2d_{i+1} + 2s_{i+1}$. At this new stage, the newly developed matured fault $\Delta d = 2d_{i+1} - 2d_i$, should not exceed the previous end zone length $2s_i$ (*i.e.* $\frac{\Delta d}{2s_i} < 1$) to avoid stress concentrations at the fault tips. For constant s/a ratios, $\frac{\Delta d}{2s_i} < 1$ can only be achieved by high propagation rates (over 30%) and/or high (over 70%) proportion of end zone length (Figure 11). Because fault propagation rates are estimated on the range of 0.25 to 2.5% (Cowie and Scholz 1992c; Peacock and Sanderson 1996), it seems highly likely that the relative end zone length increases for each fault increment to avoid stress singularities.

Insert Figure 11.

Additionally, our stress drop estimations (Figure 8) indicate that end zone length increases with larger stress drops. Also, in general, the stress drop is positively correlated with fault length: longer faults are related to increased driving stress. Finally, as predicted by Cowie and Scholz (1992b) and Scholz (1993), fracture energy G_c scales with fault length (Figure 10), with larger faults requiring higher fracture energy to propagate/slip, and more fracture energy is released at faults with longer end zone lengths. An exception for both of these general trends is fault 4, which has a similar maximum displacement to fault 3, though with three times its length (see Figure 4a). A possible explanation for these observations is that fault 4 resulted from a linkage of several pre-existing fractures that continued to slip and grow after the linkage process, whereas faults 1,2 and 3 follow the self-similar trend of isolated fractures propagating with minimum interaction with neighbouring faults. This suggests that the analysis of individual fault propagation within the CEZ framework may have a length limit: at some growing stage, coalescence and linkage of faults might correspond to the primary fault growth process. A similar interpretation is reported by Rotevatn et al. (2019) for the growth of normal faults in sedimentary rocks. Further analysis on the displacement distribution of long faults (above 5m length) would be required to confirm this hypothesis in our case study. Finally, it would be required to perform the inversion analysis presented here in datasets from other geological settings to confirm and expand our proposed fault growth model.

5.3 Implications for seismological estimations of stress drop

Our stress drop estimations form measured faults (Figure 9, ranging from 10-100 MPa) exceed the generally accepted range for seismological source stress drops calculations (*e.g.*, 0.1-10 MPa;

e.g., Abercrombie, 1995; Aki, 1967; Houston, 2001; Shearer et al., 2006). Based on observations that some microseismicity from the same location had similar seismic moments, but different sourced durations, Lin and Lapusta (2018) investigated the possibility that ignoring duration heterogeneity may yield systematically under-estimated stress drops. They considered complex source models made of heterogeneous fault patches with strong variations in shear strength due to asperities, as opposed to standard circular uniform source models showing that these source models result in a non-linear relationship between seismic moment and duration. Simulations on these complex sources yielded stress drops as much as 100 to 1000 times larger than determined by traditional seismological methods. These new source models can be interpreted as the 3D analogue to our 2D model of shear crack propagation across a fault with varying shear strength.

Our stress drop calculations magnitudes are comparable to those of Lin and Lapusta (2018) in terms of both stress drop magnitude and source complexity, suggesting that our linear regression methodology might be applicable for correlating field fault data to seismological estimations of stress drop. It is also worth pointing out that stress drops considered in this study are substantially smaller than those determined previously using similar data derived from outcrop scale mapping in the Sierra Nevada batholith (Griffith et al., 2009). However, we suggest that their results may substantially overestimate stress drop because they limited their analysis to LEFM faults.

6 Conclusions

Sixty-three strike-slip faults developed in low-porosity crystalline rock, covering a length range of five orders of magnitude, show a linear displacement to length ratio defined by the equation $\boldsymbol{d = 0.0337L^{1.02}}$, with a coefficient of determination $\boldsymbol{R^2 = 0.94}$.

The relationship between d_{max} and L obtained for this data set confirms a linear scaling between d_{max} and L, where the constant of proportionality varies with rock type and tectonic environment.

By using a multiple linear regression approach based on the cohesive end zone (CEZ) crack model by Burgmann et al., (1994), we inverted for shear tractions, endzone lengths and shear modulus from mapped slip distribution profiles. Our calculations show that best fit shear moduli increase with decreasing fault length and displacement, whereas resolved stress drop and relative end zone length increase with fault length.

Our findings suggest that the accepted paradigm in which the self-similarity of the fault growth process occurs only on the conditions of faults developing under constant remote shear stress, invariable elastic properties and constant relative length of the end zone might not be accurate. In contrast, it seems that there is a trade-off between end zone length, elastic modulus and stress drop over fault growth: as the effective elastic modulus decreases during the progressive fracturing of the medium, faults may increase end zone length and stress drop to propagate. This trade-off thus preserves the self-similarity of the system.

Our stress drop estimations correlate with recent reinterpretation of complex source models with variable in shear strength due to asperities, which suggests that our linear regression methodology can be applicable to relate field fault measurements to seismological estimates.

Acknowledgements

JC and TM acknowledge the help of Gloria Arancibia, Gabriel Gonzalez, Dan Faulkner, Pamela Perez, Rodrigo Gomila and Gert Heuser over many years of work in the Atacama Fault System. Maria Paz Reyes Hardy, Rocio Quilaleo, and Kevin Quinzacara (Universidad Católica del Norte) helped obtaining fault parameters in the field. Becky Pearce kindly helped by checking structural map measurements. ASY acknowledges the support of CONICYT for the Chile Scholarship for International PhD studies. Fondecyt Projects 1020436, 1110464 and 1141139 and CONICYT FONDAP Program through Grant No. 1511017 have funded our work over the last 10 years. We are very thankful for the thorough review by two anonymous reviewers and Associate Editor Dr Stephen Laubach, which helped to considerably improve the manuscript.

References

Aben, F. M., Brantut, N., Mitchell, T. M., and David, E. C. (2019). Rupture energetics in crustal rock from laboratory-scale seismic tomography. Geophysical Research Letters, 46, 7337–7344. https://doi.org/10.1029/2019GL083040.

Abercrombie, R. E. (1995). Earthquake source scaling relationships from− 1 to 5 ML using seismograms recorded at 2.5-km depth. Journal of Geophysical Research: Solid Earth, 100(B12), 24015-24036.

Anders, M. H., Laubach, S. E., and Scholz, C. H. (2014). Microfractures: A review. Journal of Structural Geology, 69, 377-394. doi:10.1016/j.jsg.2014.05.011.

Aki, K. (1967). Scaling law of seismic spectrum. Journal of geophysical research, 72(4), 1217-1231.

Barenblatt, G. I. (1962). The mathematical theory of equilibrium cracks in brittle fracture. Advances in applied mechanics, 7, 55-129.

Bistacchi, A., W. A. Griffith, S. A. Smith, G. Di Toro, R. Jones, and S. Nielsen. (2011). Fault roughness at seismogenic depths from LIDAR and photogrammetric analysis, Pure and Applied Geophysics, 168 (12), 2345–2363.

Brown, M., Díaz F., Grocott, J. (1993). Displacement history of the Atacama Fault System, 25°00'S -27°00'S, northern Chile. Geological Society of America Bulletin, 105, 1165-1174.

Burgmann, R., Pollard, D.D., Martel, S.J. (1994). Slip distributions on faults: effects of stress gradients, inelastic deformation, heterogeneous host-rock stiffness, and fault interaction. Journal of Structural Geology, 16, 1675-1690.

Cartwright J. A., Trudgill B. D., Mansfield C. M., (1995). Fault growth by segment linkage: an explanation for scatter in maximum displacement and trace length data from the Canyonlands Grabens of S.E. Utah. Journal of Structural Geology, 17, 1319–1326.

Cembrano, J., González, G., Arancibia, G., Ahumada, I., Olivares, V., Herrera, V. (2005). Fault zone development and strain partitioning in an extensional strike-slip duplex: A case of study from the Mesozoic Atacama fault system, Northern Chile, Tectonophysics, 400, 105-125.

Cladouhos, T. T., & Marrett, R. (1996). Are fault growth and linkage models consistent with power-law distributions of fault lengths? Journal of Structural Geology, 18(2-3), 281–293. doi:10.1016/s0191-8141(96)80050-2.

Cotterell, B. and Rice, J.R. (1980). Slightly Curved or Kinked Cracks. International Journal of Fracture, 6, 155-169.

Cowie, P.A., Scholz, C.H. (1992a). Displacement-length scaling relationship for faults: data synthesis and discussion. Journal of Structural Geology, 14, 1149–1156. https://doi.org/10.1016/0191-8141(92)90066-6

Cowie, P.A., Scholz, C.H. (1992b). Physical explanation for the displacement-length relationship of faults using a post-yield fracture mechanics model. Journal of Structural Geology, 14, 1133–1148. https://doi.org/10.1016/0191-8141(92)90065-5.

Cowie and Scholz, (1992c). Growth of faults by accumulation of seismic slip. Journal of Geophysical Research, 97, pp. 11085-11095

Cowie, P. A., & Shipton, Z. K. (1998). Fault tip displacement gradients and process zone dimensions. Journal of Structural Geology, 20(8), 983-997.

Crider, J.G., Peacock, D.C.P. (2004). Initiation of brittle faults in the upper crust: a review of field observations. Journal of Structural Geology, 26, 691-707.

Dawers, N.H., Anders, M.H., and Scholz, C.H. (1993). Growth of normal faults: Displacement-length scaling, Geology, 21, 1107-1110.

Dugdale, D. S. (1960). Yielding of steel sheets containing slits. Journal of the Mechanics and Physics of Solids, 8(2), 100-104.

Erdogan, F., Sih, G.C. (1963). On the crack extension in plates under plane loading and transverse shear. Journal of Basic Engineering, Transactions of American Society of Mechanical Engineers, 85, 519-527.

Faulkner, D.R., Mitchell, T.M., Jensen, E., Cembrano, J. (2011). Scaling of fault damage zones with displacement and the implications for fault growth processes. Journal of Geophysical Research, 116, B05403.

Faulkner, D. R., Mitchell, T. M., Healy, D., & Heap, M. J. (2006). Slip on'weak'faults by the rotation of regional stress in the fracture damage zone. Nature, 444(7121), 922.

Gillespie, P.A., Walsh, J.J., Watterson, J. (1992). Limitations of dimension and displacement data from single faults and the consequences for data analysis and interpretation. Journal of Structural Geology, 14, 1157–1172. https://doi.org/10.1016/0191-8141(92)90067-7

González, G. (1996). Evolución tectónica de la Cordillera de la Costa de Antofagasta (Chile): Con especial referencia las deformaciones sinmagmáticas del Jurásico Cretácico Inferior. Ph.D thesis. Berliner Geowissenschaftliche Abhandlungen (A), Band 181, 111 p.

Goodier, J. N., & Field, F. A. (1963). Fracture of solids. Inter. Pub., New York, p103.

Griffith, W.A., Di Toro, G., Pennacchioni, G., Pollard, D.D., Nielsen, S. (2009). Static stress drop associated with brittle slip events on exhumed faults. Journal of Geophysical Research: Solid Earth 114, 1–13. https://doi.org/10.1029/2008JB005879

Gupta, A. and Scholz, C. H. (2000). A model of normal fault interaction based on observations and theory. Journal of Structural Geology, 22(7), 865-879. https://doi.org/10.1016/S0191-8141(00)00011-0

Healy, D., Jones, RR. & Holdsworth, RE. (2006). Three-dimensional brittle shear fracturing by tensile crack interaction. Nature, 439, 64-67.

Heap, M. J., & Faulkner, D. R. (2008). Quantifying the evolution of static elastic properties as crystalline rock approaches failure. International Journal of Rock Mechanics and Mining Sciences, 45(4), 564-573.

Heap, M. J., Vinciguerra, S., & Meredith, P. G. (2009). The evolution of elastic moduli with increasing crack damage during cyclic stressing of a basalt from Mt. Etna volcano. Tectonophysics, 471(1-2), 153-160.

Herrera, V., Cembrano, J., Olivares, V., Kojima, S., Arancibia, G. (2005). Precipitation by depressurization and boiling in veins hosted in an extensional strike-slip duplex: microstructural and microthermometric evidence. Revista Geologica De Chile, 32 (2), 207-227.

Houston, H. (2001). Influence of depth, focal mechanism, and tectonic setting on the shape and duration of earthquake source time functions. Journal of Geophysical Research: Solid Earth, 106(B6), 11137-11150.

Jensen, E., Cembrano, J., Faulkner, D., Veloso, E., Arancibia, G. (2011). Development of a self-similar strike-slip duplex system in the Atacama Fault system, Chile. Journal of Structural Geology, 33, https://doi.org/10.1016/j.jsg.2011.09.002

Kim, Y.S., Sanderson, D.J. (2005). The relationship between displacement and length of faults: A review. Earth-Science Reviews, 68, 317–334. https://doi.org/10.1016/j.earscirev.2004.06.003

Kanninen, M. F., and Popelar, C. H. (1985). Advanced fracture mechanics (No. 15). Oxford University Press.

Laubach, S.E., Eichhubl, P. Hargrove, P., Ellis, M.A., Hooker, J.N., (2014). Fault core and damage zone fracture attributes vary along strike owing to interaction of fracture growth, quartz accumulation, and differing sandstone composition. Journal of Structural Geology 68, Part A, 207-226. doi: 10.1016/j.jsg.2014.08.007

Laubach, S. E., Lander, R. H., Criscenti, L. J., Anovitz, L. M., Urai, J. L., Pollyea, R. M., ... & Olson, J. E. (2019). The role of chemistry in fracture pattern development and opportunities to advance interpretations of geological materials. Reviews of Geophysics.doi:10.1029/2019RG000671.Lin, Y. Y., and Lapusta, N. (2018). Microseismicity simulated on asperity-like fault patches: On scaling of seismic moment with duration and seismological estimates of stress drops. Geophysical Research Letters, 45(16), 8145-8155.

Lockner, D.A., Byerlee, J.D., Kuksenko, V., Ponomarev, A., Sidorin, A. (1991). Quasi-static fault growth and shear fracture energy in granite. Nature, 350 (6313), 39-42.

Manighetti, I., Campillo, M., Sammis, C., Mai, P. M., & King, G. (2005). Evidence for self-similar, triangular slip distributions on earthquakes: Implications for earthquake and fault mechanics. Journal of Geophysical Research: Solid Earth, 110(B5). https://doi.org/10.1029/2004JB003174

Marrett, R., Allmendinger, R.W. (1991). Estimates of strain due to brittle faulting: sampling of fault populations. Journal of Structural Geology, 13, 735–738.

Martel, S.J., Pollard, D.D., Segall, P. (1988). Development of simple strike-slip fault zones, Mount Abbot Quadrangle, Sierra Nevada, California. Bulletin of the Geological Society of America, 100, 1451-1465.

Mitchell, T.M., Faulkner, D.R. (2009). The nature and origin of off-fault damage surrounding strike-slip fault zones with a wide range of displacements: A field study from the Atacama fault system, northern Chile. Journal of Structural Geology, 31, 802–816. https://doi.org/10.1016/j.jsg.2009.05.002

Moore, D. E., & Lockner, D. A. (1995). The role of microcracking in shear-fracture propagation in granite. Journal of Structural Geology, 17(1), 95-114.

Muraoka, H., & Kamata, H. (1983). Displacement distribution along minor fault traces. Journal of Structural Geology, 5(5), 483-495..

Olivares, V., Cembrano, J., Arancibia, G., Reyes, N., Herrera, V., & Faulkner, D. (2010). Tectonic significance and hydrothermal fluid migration within a strike-slip duplex fault-vein network: an example from the Atacama Fault System. Andean Geology, 37(2), 473-497.

Palmer, A. C., & Rice, J. R. (1973). The growth of slip surfaces in the progressive failure of over-consolidated clay. Proceedings of the Royal Society of London. A. Mathematical and Physical Sciences, 332(1591), 527-548.

Peacock, D. C. P., & Sanderson, D. J. (1996). Effects of propagation rate on displacement variations along faults. Journal of Structural Geology, 18(2-3), 311-320.

Peacock, D.C.P. (2001). The temporal relationship between joints and faults. Journal of Structural Geology, 23, 329– 341.

Pollard, D.D., Segall, P. (1987). Theoretical displacements and stresses near fractures in rock: with applications to faults, joints, veins, dikes, and solution surfaces. In: Atkinson, B.K. (Ed.), Fracture Mechanics of Rock. Academic Press, London, 277-349.

Rotevatn, A., Jackson, C. A. L., Tvedt, A. B., Bell, R. E., and Blækkan, I. (2019). How do normal faults grow?. Journal of Structural Geology, *125*, 174-184.

Scheuber, E., González, G. (1999). Tectonics of the Jurassic–Early Cretaceous magmatic arc of the north Chilean Coastal Cordillera (228–268S): a story of crustal deformation along a convergent plate boundary. Tectonics, 18, 895–910.

Schlische, R. W., Young, S. S., Ackermann, R. V., & Gupta, A. (1996). Geometry and scaling relations of a population of very small rift-related normal faults. Geology, 24(8), 683-686.

Scholz, C.H., Dawers, N.H., Yu, J.-Z., Anders, M.H., Cowie, P.A. (1993). Fault growth and fault scaling laws: Preliminary results. Journal of Geophysical Research: Solid Earth, 98, 21951–21961. https://doi.org/10.1029/93JB01008

Scholz, C. H., and Lawler, T. M. (2004). Slip tapers at the tips of faults and earthquake ruptures. Geophysical research letters, 31(21).

Scholz, C. H. (2019). The mechanics of earthquakes and faulting. Cambridge university press.

Segall, P., Pollard, D.D. (1983). Nucleation and growth of strike slip faults in granite. Journal of Geophysical Research, 88, 555-568.

Segall, P., and D. Pollard. (1980). Mechanics of Discontinuous Faults, J. Geophys. Res, 85(B8), 4337-4350.

Shearer, P. M., Prieto, G. A., and Hauksson, E. (2006). Comprehensive analysis of earthquake source spectra in southern California. Journal of Geophysical Research: Solid Earth, 111(B6).

Smith, D. L., and Evans, B. (1984). Diffusional crack healing in quartz. Journal of Geophysical Research: Solid Earth, 89(B6), 4125-4135.

Tada, H., Paris, P. C., and Irwin, G. R. (2000). The stress analysis of cracks handbook. American Society of Mechanical Engineers, Third Edition. Park Avenue, New York, NY, 10016.

Tenthorey, E., Cox, S. F., and Todd, H. F. (2003). Evolution of strength recovery and permeability during fluid–rock reaction in experimental fault zones. Earth and Planetary Science Letters, 206(1-2), 161-172.

Vermilye, J.M., Scholz, C.H. (1998). The process zone: a microstructural view of fault growth. Journal of Geophysical Research, 103, 12223-12237.

Wilson, J.E., Chester, J.S., Chester, F.M. (2003). Microfracture analysis of fault growth and wear processes, Punchbowl Fault, San Andreas system, California. Journal of Structural Geology, 25, 1855-1873.

Walsh, J.J., Watterson, J. (1988). Analysis of the relationship between displacements and dimensions of faults. Journal of Structural Geology, 10, 239–247. https://doi.org/10.1016/0191-8141(88)90057-0

Willemse, E.J. and Pollard, D.D. (1998). On the orientation and patterns of wing cracks and solution surfaces at the tips of a sliding flaw or fault. Journal of Geophysical Research: Solid Earth, 103(B2), 2427-2438.

Xu, S.S., Nieto-Samaniego, A.F., Alaniz-Álvarez, S.A., Velasquillo-Martínez, L.G. (2006). Effect of sampling and linkage on fault length and length-displacement relationship. International Journal of Earth Sciences, 95, 841–853. https://doi.org/10.1007/s00531-005-0065-3.

Zang, A., Wagner, F.C., Stanchits, S., Janssen, C., and Dresen, G. Fracture process zone in granite. J. Geophys. Res, 105 (B10), 23651–23661.

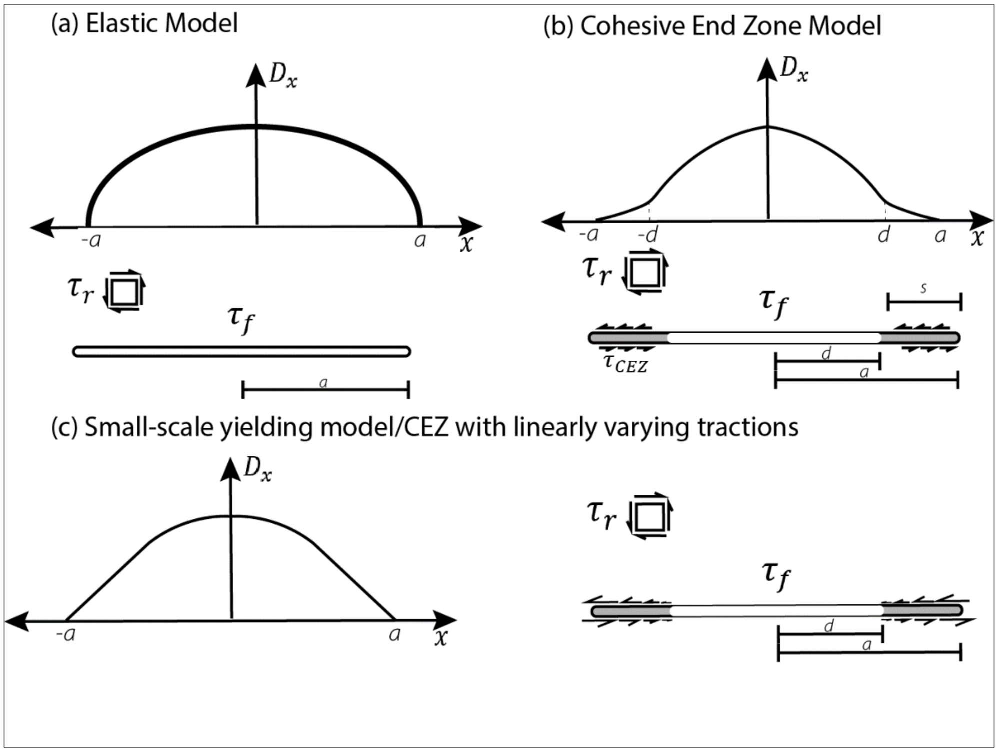

Figure 1. (a) Linear Elastic model of a crack of length 2a subjected to a uniform stress drop $\tau_r - \tau_f$ *and resulting elliptical slip distribution, (b) Cohesive End Zone model of a crack of length 2a with a cohesive end zone of length 2s and resulting slip distribution tapering towards the crack tips, (c) Slip distribution for small scale yielding model or Constant Fault Tip Taper. A similar distribution is obtained from a CEZ model with linearly varying tractions (Modified from Scholz 2019).*

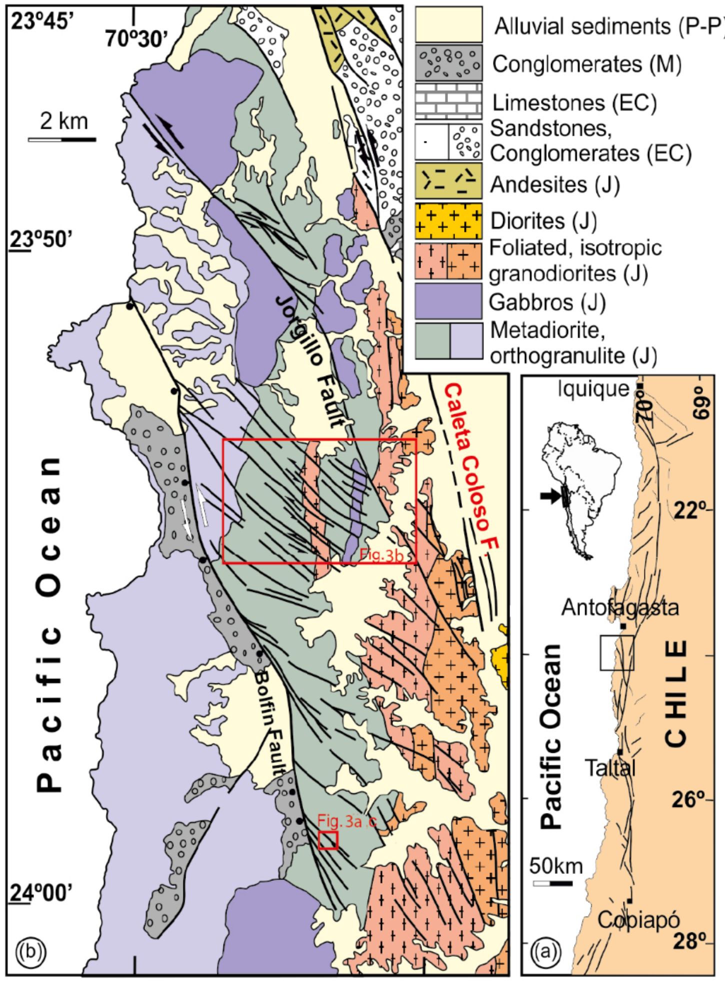

Figure 2. Regional geological and structural map of the Caleta Coloso Duplex (CCD) in the Atacama fault system (AFS), northern Chile. Isotropic igneous and high-grade metamorphic rocks dominate the CCD geology. First and second-order faults of the CCD are highlighted. Insets show locations for Figures 3a, b and c.

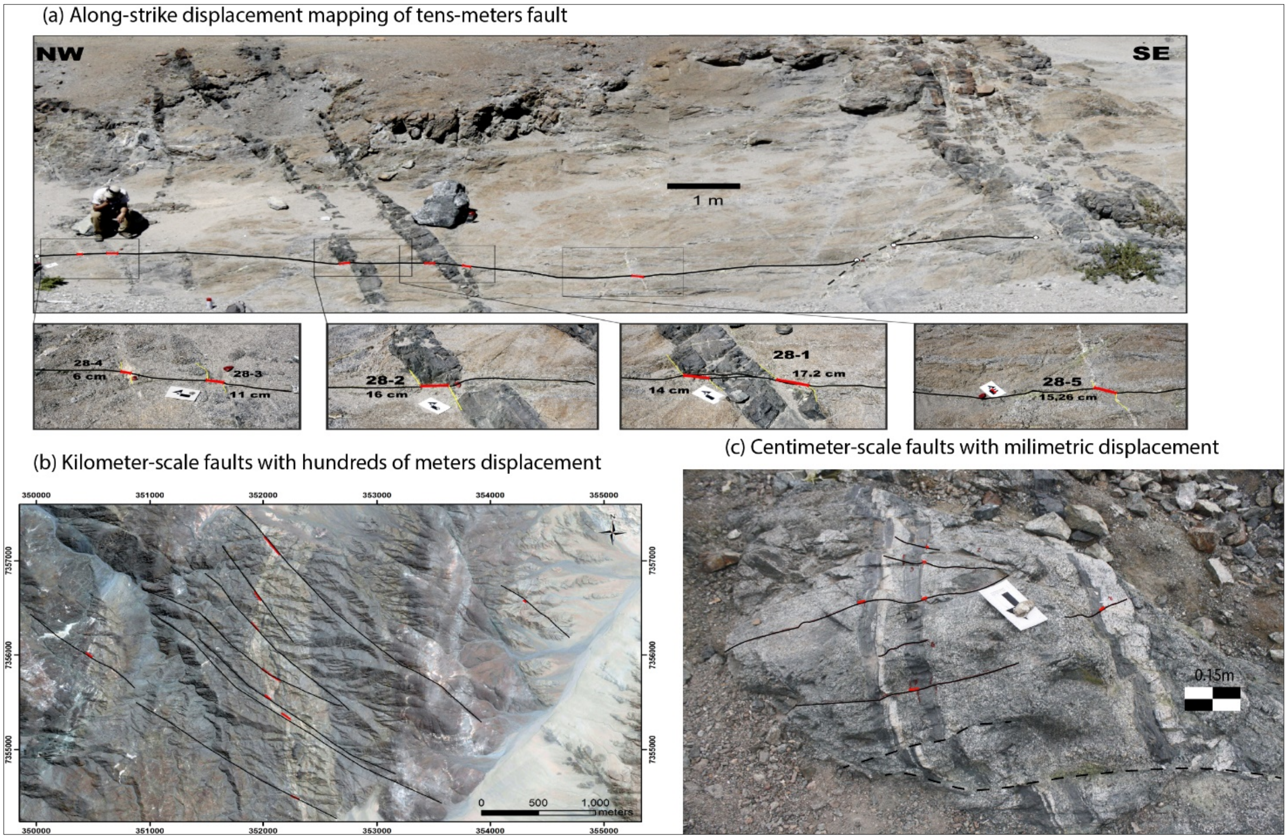

Figure 3.(a) Along-strike displacement measurement of tens of meters long strike slip fault (black), from offset (red) in sub-vertical dykes. (b) Satellite image showing kilometer-scale faults (black) with hundreds of meter displacement (red). (c)Centimeter-scale faults with millimetric displacement. All maps are in plan views. See figure 1 for locations of a, b and c.

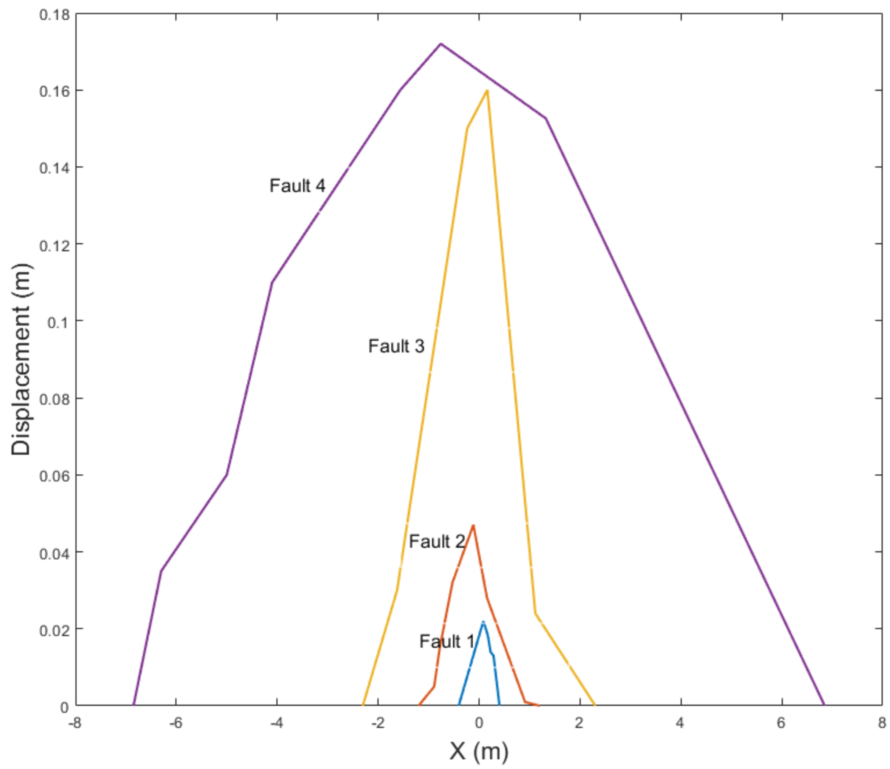

Figure 4. Fault displacement profiles of four faults for which several displacement markers were identified. X correspond to distance with respect to the fault center.

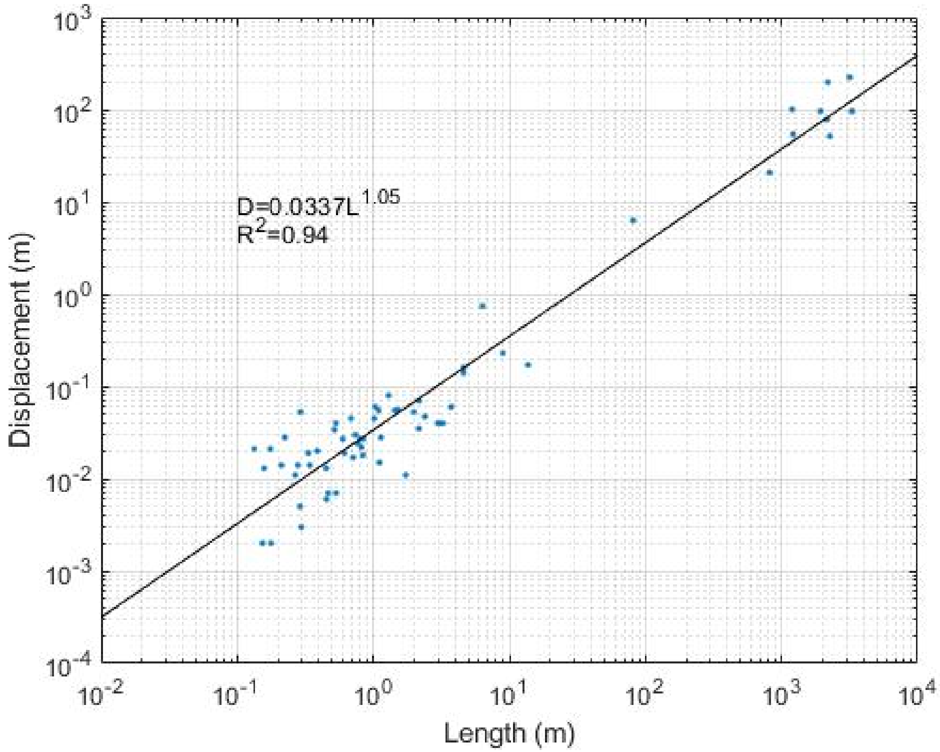

Figure 5. Displacement vs Length in a log-log plot, covering a range of five orders of magnitude. Power-law fit line indicates exponent of 1.02 with a coefficient of determination 0.94.

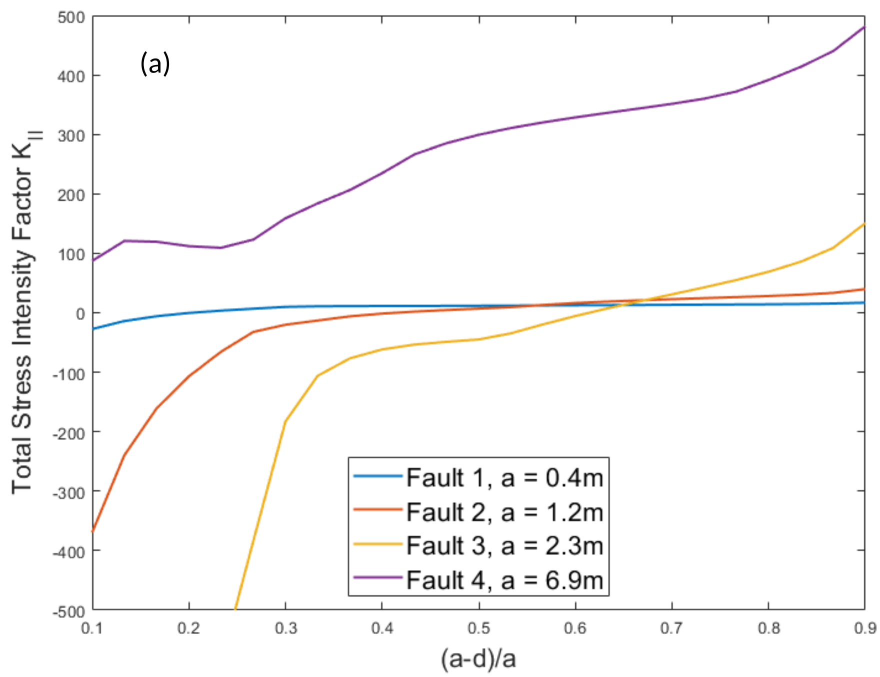
(a)
Total Stress Intensity Factor K_{II}
(a-d)/a
Fault 1, a = 0.4m
Fault 2, a = 1.2m
Fault 3, a = 2.3m
Fault 4, a = 6.9m
500
400
300
200
100
0
-100
-200
-300
-400
-500
0.1
0.2
0.3
0.4
0.5
0.6
0.7
0.8
0.9

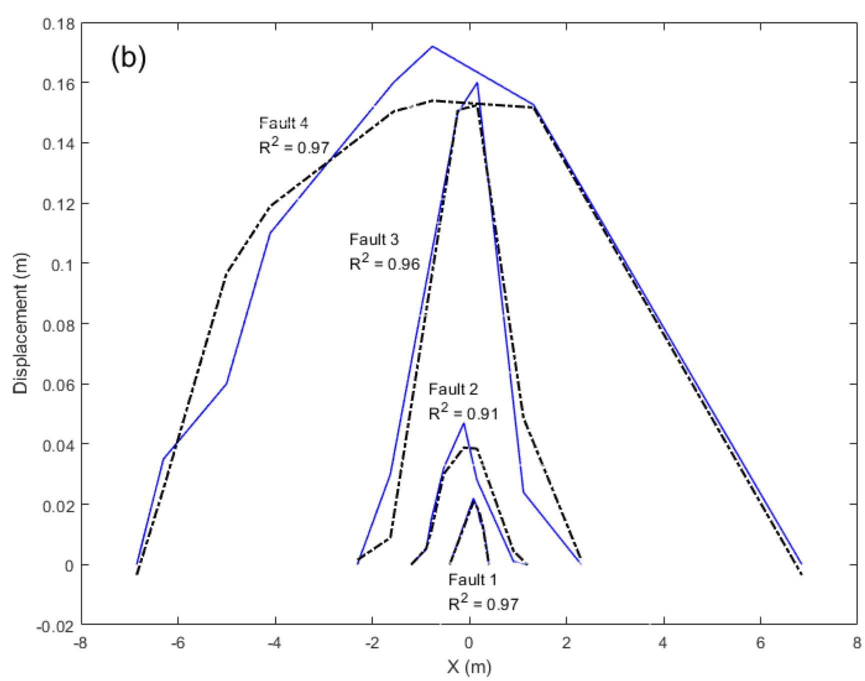
(b)
Displacement (m)
X (m)
Fault 4
R^2 = 0.97
Fault 3
R^2 = 0.96
Fault 2
R^2 = 0.91
Fault 1
R^2 = 0.97
0.18
0.16
0.14
0.12
0.1
0.08
0.06
0.04
0.02
0
-0.02
-8
-6
-4
-2
0
2
4
6
8

Figure 6.(a) K_{II}^{total} *as a function of relative end zone length* $(a-d)/a$. *(b) Modelled slip distributions (dashed black) fitting measured slip profiles (blue, same as Figure 4). The coefficient of determination* R^2 *is shown for every fit. See text for details.*

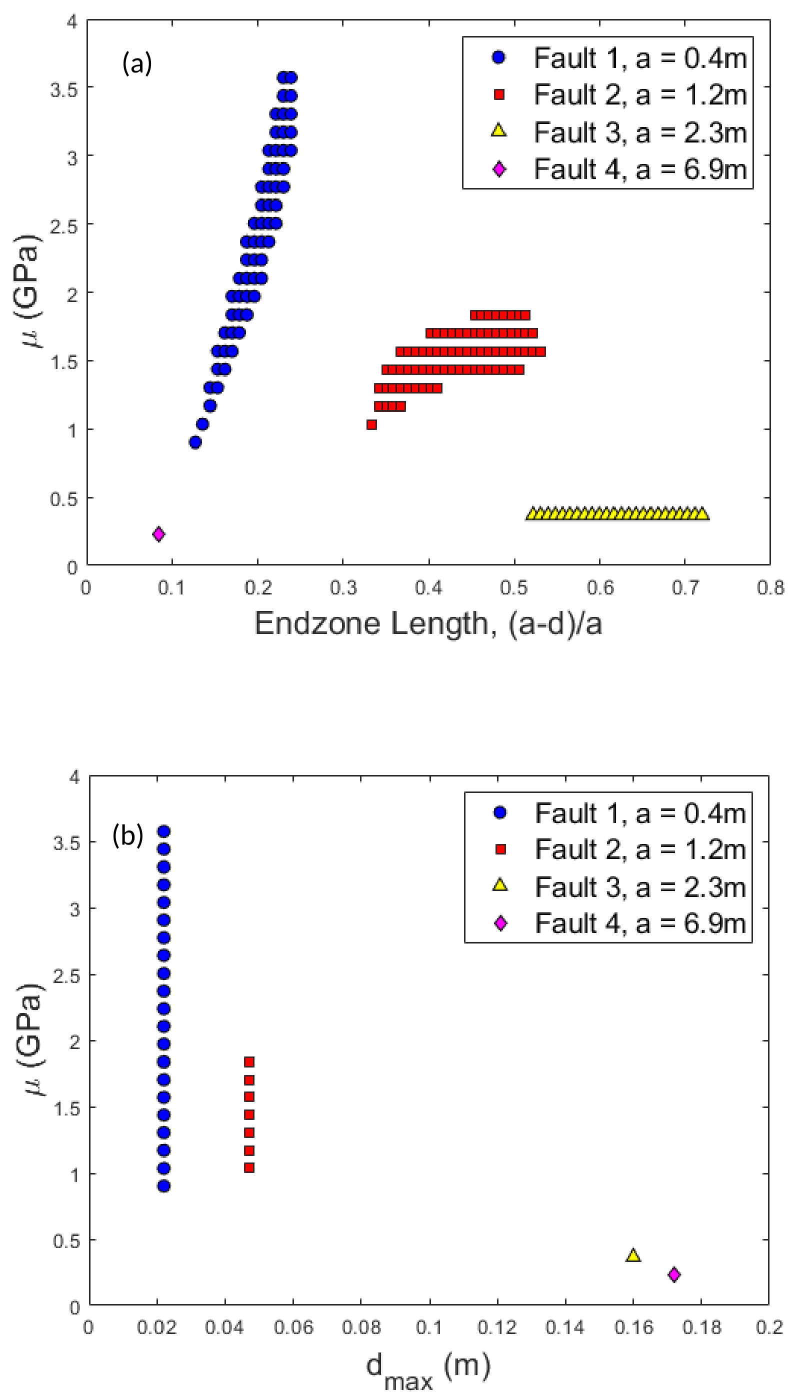

Figure 7. (a) Shear moduli (GPa) as a function of end zone length for each fault. Each circle plotted represents a combination of parameters that meet the defined criteria. Shorter faults (Faults 1 and 2) are consistent with higher shear moduli than those of longer faults (Faults 3 and 4).(b) Shear modulus as a function of maximum fault displacement. Shear modulus consistently decreases with increasing displacement.

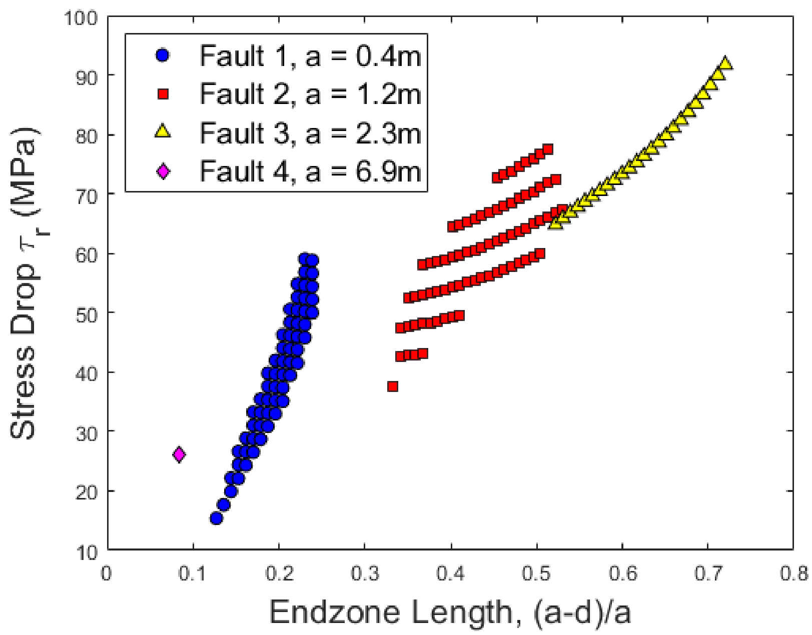

Figure 8. Stress drop as a function of end zone length for each modelled fault. Larger stress drops require larger end zone lengths. Also, longer faults are associated with larger stress drops. An exception for this trend is fault 4.

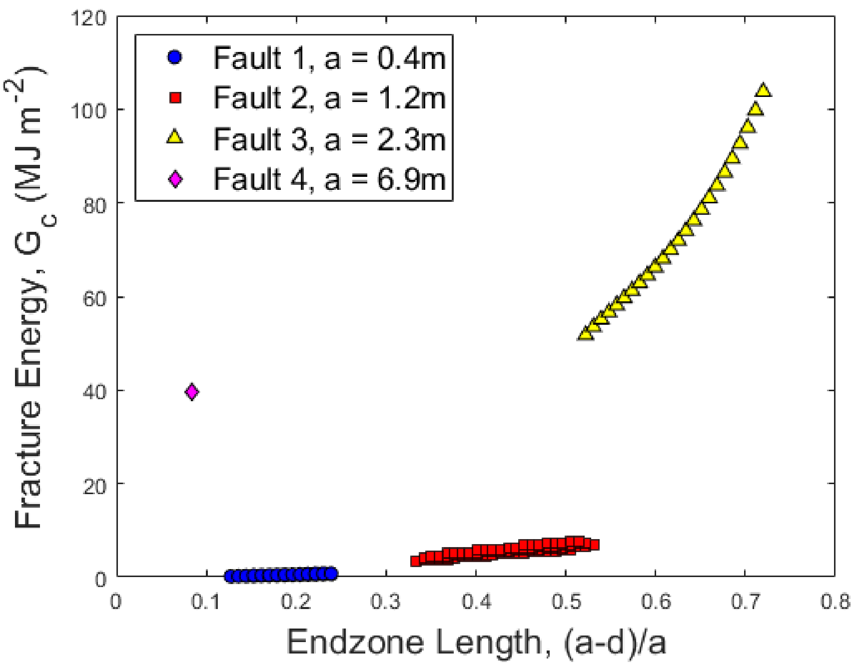

Figure 6. Fracture energy as a function of end zone length for each fault. In general, more fracture energy is required for propagating cracks with longer end zone lengths. G_c *scales with fault length, with larger faults requiring higher fracture energy to propagate/slip. An exception for this trend is fault 4.*

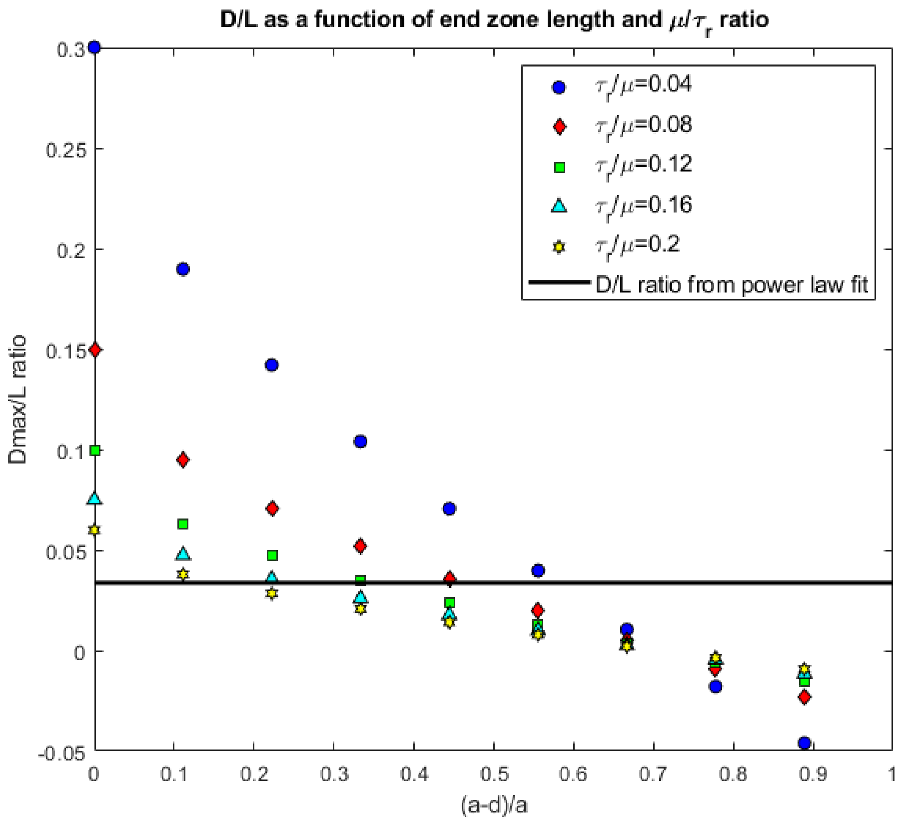

Figure 10. D/L ratio as a function of end zone lengths length for various combinations of τ_r and μ, represented by the τ_r/μ ratio. The characteristic d_{max}/L ratio calculated for our case study is shown in balck. Increasing end zone lengths correlate with decreasing d_{max}/L ratios. Also, increasing d_{max}/L ratios are related to increasing shear moduli and decreasing remote shear stresses, showing that multiple combinations of parameters result in the characteristic d_{max}/L.

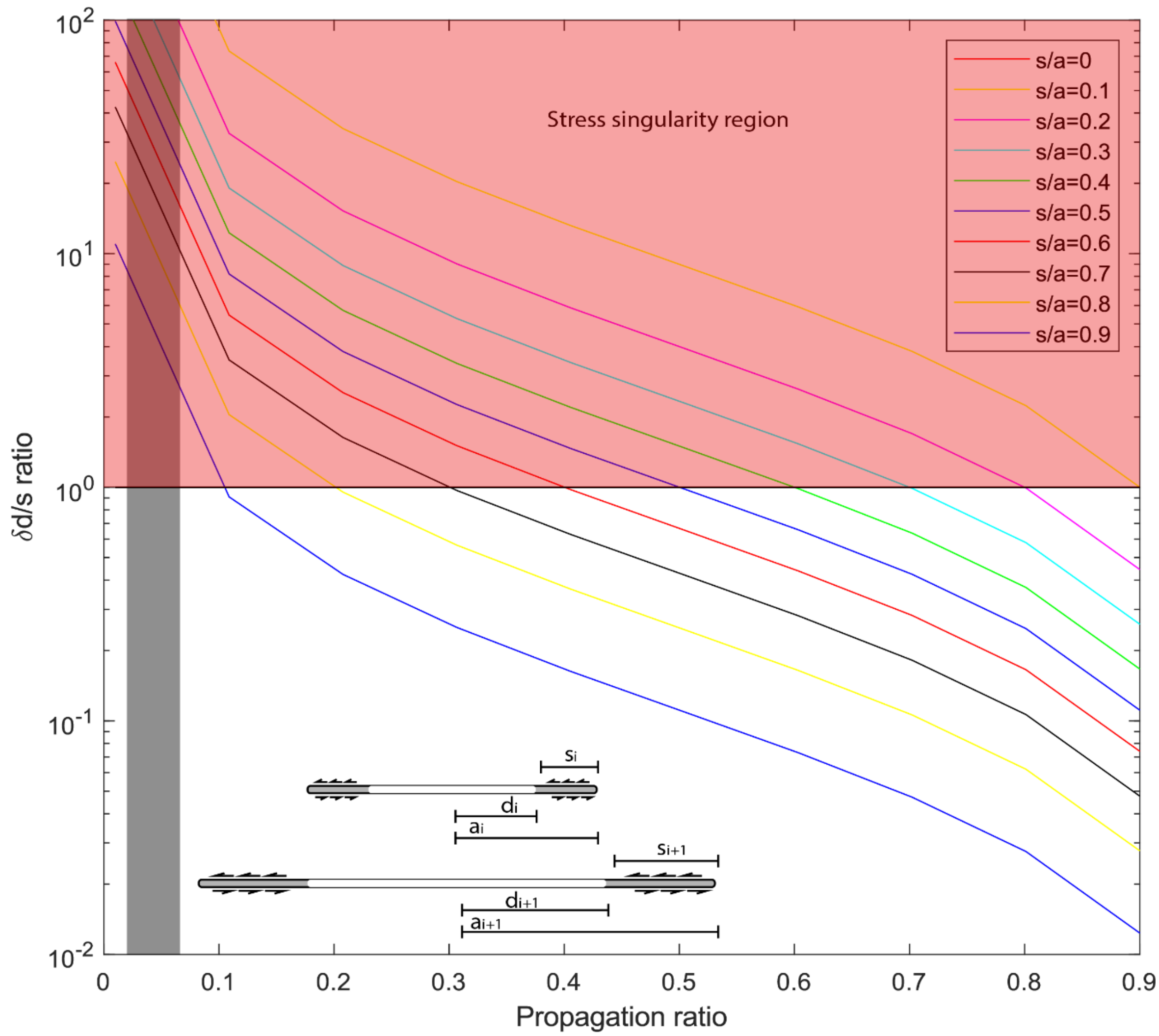

Figure 11. $\frac{\Delta d}{s_i}$ *ratio as a function of propagation ratio for various constant s/a ratios.* $\frac{\Delta d}{s_i} > 1$ *imply that between growing stages i and i+1, the newly developed mature segment of the fault* (Δd) *exceed the previous end zone length* (s_i)*, resulting in a stage without end zone that produces a stress singularity at the fault tips and contradicts the CEZ model.* $\frac{\Delta d}{s_i} < 1$ *can only be achieved by high propagation ratio, much higher than the*

estimated range of 0.25 to 2.5% (Cowie and Scholz 1992c; Peacock and Sanderson 1996), shown approximately in grey rectangle, or high s/a ratios.